

Simulation of directional solidification, thermochemical convection, and chimney formation in a Hele-Shaw cell

Richard F. Katz^{a,b,*}, M. Grae Worster^b

^a Department of Earth Sciences, University of Oxford, Parks Road, Oxford OX1 3PR, United Kingdom

^b Institute of Theoretical Geophysics, Department of Applied Mathematics and Theoretical Physics, Wilberforce Road, Cambridge CB3 0WA, United Kingdom

ARTICLE INFO

Article history:

Received 1 February 2008

Received in revised form 30 May 2008

Accepted 26 June 2008

Available online 11 August 2008

PACS:

47.11.–j

44.25.+f

47.20.Bp

47.15.gp

81.30.Fb

Keywords:

Convection

Solidification

Chimneys

Reactive flow

Mushy layers

Numerical methods

PETSc

Casting

Ammonium chloride

ABSTRACT

We have developed fully resolved, two-dimensional, finite volume simulations of directional solidification of a binary alloy in a Hele-Shaw cell. Use of Darcy's law and the Enthalpy Method throughout the computational domain allows us to avoid prescribing internal boundary conditions on the interfaces between solid, mushy, and liquid regions. We present a description of the theoretical model, computational approach, two reduced benchmark calculations, and simulations of the full governing equations. In simulations with parameter values that approximate experiments, boundary-layer-mode convection produces corrugations in the mush–liquid interface. Some of these corrugations become chimneys that grow and interact within the mushy layer. We consider two porosity–permeability relations and examine their consequences for chimney spacing and mushy layer height. Our results are broadly similar to experiments on directional solidification of NH_4Cl [S.S.L. Peppin, H.E. Huppert, M.G. Worster, Steady-state solidification of aqueous ammonium chloride, *J. Fluid Mech.* 599 (2008) 465–476; S.H. Whiteoak, H. Huppert, M.G. Worster, Conditions for defect-free solidification of aqueous ammonium chloride in a quasi 2d directional solidification facility, *J. Cryst. Growth* (2008)]. We describe other simulations that are tuned to suppress boundary layer mode convection and that, instead, go unstable by the mushy layer mode [M.G. Worster, Instabilities of the liquid and mushy regions during solidification of alloys, *J. Fluid Mech.* 237 (1992) 649–669]. We investigate the morphological evolution of the mush well beyond the linear instability regime.

© 2008 Elsevier Inc. All rights reserved.

1. Introduction

Solidification of multi-component melts from a cold boundary generally gives rise to a solid–liquid interface that is unstable to the growth of crystalline dendrites [30]. The ensemble of dendrites forms a porous, permeable mushy layer [49]. In general, crystals have a composition different from their parental melt, so solidification leads to changes in solute concentration of the melt in a narrow region around the crystals. Changes in solute concentration correspond to changes in melt density. In some cases [48], this causes compositional convection to occur within the mushy region. Reactions between moving melt and the dendritic matrix lead to the formation of chimneys of zero-solid-fraction and to focusing of flow into these chimneys. This instability is observed in a wide variety of systems from industrial (e.g. casting [17,24]) to natural (e.g. for-

* Corresponding author. Address: Department of Earth Sciences, University of Oxford, Parks Road, Oxford OX1 3PR, United Kingdom.
E-mail address: Richard.Katz@earth.ox.ac.uk (R.F. Katz).

mation of sea ice [44]). In the casting of turbine blades, chimneys represent defects that weaken the final product; in sea ice, chimneys allow for enhanced drainage of concentrated brine and hence have important implications for oceanic deep water formation. A thorough understanding of the dynamics of convection in mushy layers is thus of great interest and wide applicability.

Laboratory experiments on the solidification of two-component liquids are a primary tool for investigating mushy layer dynamics. In experiments, the fluid is typically contained in a tank whose top or bottom is cooled to a temperature below the liquidus. Because the cold boundary is stationary, such experiments are termed “fixed chill.” Although solutions of NaCl–water [44], sugar–water [3], and alcohol–water [48], as well as metallic alloys [10], have been used in experiments, aqueous ammonium chloride is most common. This is because NH_4Cl crystallizes over a temperature range easily accessible in the laboratory and forms dendrites that are similar to those formed from metallic alloys. Chimney formation in fixed chill experiments on NH_4Cl has been well studied (e.g. [41,42,13]). Theoretical models of chimney formation, however, have typically been derived under conditions of directional solidification rather than fixed chill.

Directional solidification refers to a system in which a liquid-filled container is moved through a device that chills it, causing a freezing front to propagate through the liquid at the same rate as but in the opposite direction to the motion of the container. An experimental apparatus for directional solidification was recently developed to provide a better correspondence between experiments and mushy layer theory [33]. It consists of a vertical, fluid-filled Hele-Shaw cell that is translated through two sets of fixed-temperature heat exchangers, one set warm, the other cold. The heat exchangers impose a vertical temperature gradient in the fluid. Solidification progresses from the cold end toward the warm end and, eventually, an equilibrium mushy layer height is reached [34,45]. Fig. 1 shows an image of light transmitted through the mushy layer of an experiment that has reached an approximately steady mushy layer height. Darker regions correspond to lower porosity, chimneys appear as lighter, vertical bands.

Profiles of steady-state temperature, porosity and concentration have been predicted theoretically for the case of directional solidification with no fluid motion [21,19]. Worster [47] studied the linear instability of this basic state with simple constitutive equations for permeability. This work demonstrated the existence of two modes of convective instability. At longer wavelengths, convective cells penetrate to the bottom of the mushy layer, while at shorter wavelengths, convection is mainly confined to the liquid region. The long-wavelength mushy layer mode seems the obvious candidate to explain the formation of chimneys, however neither experiments nor stability analysis confirm this conclusively. To model the evolution of convection and the development of chimneys requires an analysis that captures all the nonlinearities in the governing equations.

Past models that incorporate nonlinearities have typically been used to look for steady-state solutions with prescribed chimney locations (e.g. [36,29,16]). While interesting, such models cannot elucidate the path to chimney formation, nor can they investigate the dynamical interactions between chimneys. These goals require a time-dependent solution to the governing equations. Owing to the complexity of the full equations, such a solution can only be obtained numerically. While numerical simulations are more difficult to interpret than analytical solutions, they offer several advantages. Among these

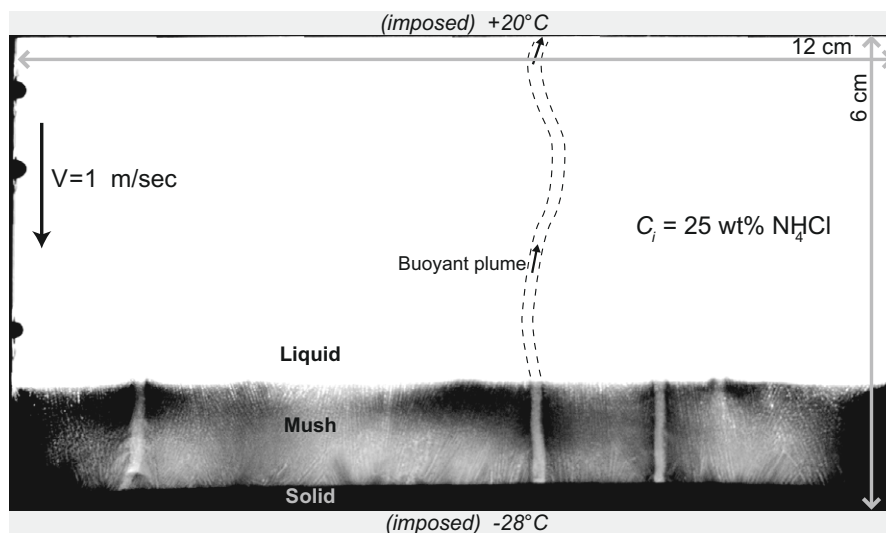


Fig. 1. An example of directional solidification of NH_4Cl in the laboratory. This image was acquired when the mushy layer had reached a constant height above the bottom heat exchanger, about 220 min after the start of the experiment. The Hele-Shaw cell is illuminated from behind. The initial concentration is 25 wt% NH_4Cl , the translation rate of the cell is 1 $\mu\text{m/s}$ downward, and the temperature at the top and bottom heat exchangers is 20 and -28°C , respectively. Three chimneys are clearly visible on the near side of the cell and several others are obscured because they are adjacent to the far side. A plume of chemically buoyant fluid rises out of each chimney although, because of the lighting, these are not visible here (see images in [34,45]).

are (i) the ability to study both the onset of instability and the dynamics of fully developed convection, (ii) the ability to generate time-dependent patterns of porosity and flow and (iii) the ability to test different, nonlinear constitutive laws for permeability. Below we illustrate these three points using new results obtained from our simulations.

The development of a useful numerical simulation of mushy layer dynamics has been a challenge for two important reasons. The first of these stems from the typical approach of splitting the computational domain into subdomains for the solid, mushy and liquid regions in which different equations are solved. In such simulations, boundary conditions must be specified between subdomains and, of particular importance, on the mush–liquid interface. A split-domain approach was taken by Schulze and Worster [36,37] and by Chung and Worster [16]. The latter solved for steady-state convection and self-consistently determined the position of the mush–liquid interface. In their simulation, however, chimney spacing was specified *a priori* and chimneys were not allowed to interact or evolve. To circumvent this limitation, other workers have formulated the problem with a single domain approach where the local properties depend on a phase-field variable [32,9,11,22]. We have adopted such an approach and hence we solve the same equations over the entire domain. We do not prescribe any aspect of the mushy layer structure.

A second impediment on the development of useful numerical simulations of convection in mushy layers stems from the ascent rate of buoyant plumes in the open liquid region. Plumes emanating from the mushy layer or its compositional boundary layer are highly buoyant. These plumes ascend very rapidly if conservation of momentum in the open liquid region is modeled with the Navier–Stokes equation (or with the Darcy–Brinkman equation [28]). Since the simulation time-step is limited by the largest velocity within the domain, high ascent rates can lead to time-steps that are minuscule compared to the timescale of evolution of the mushy layer. This makes it prohibitively expensive to integrate the equations over a dimensional time interval that is comparable to that of experiments. Since recent experiments have been performed within a narrow gap between glass plates, a Hele–Shaw cell, it is reasonable to assume that conservation of momentum is described by Darcy’s law throughout the domain. This provides a control on the ascent rate of plumes in the liquid region by adjusting the gap width of the Hele–Shaw cell and hence the permeability at zero solid fraction. While the experimental cell has a gap width of 5 mm, the diameter of typical plumes in experiments is smaller than this. Hence our use of Darcy’s law, while convenient, is not entirely justified in the context of those experiments. We examine the validity of this choice in Section 5.

In Section 2, we describe the mathematical formulation of the model and give an overview of its numerical implementation. In Section 3, we consider two benchmark cases that validate the thermodynamics and fluid dynamics modeled by our code. In Section 4, we describe representative results of simulations of two types. The first type is calibrated to mimic experiments while the second type is calibrated to demonstrate the mushy layer mode of instability. Section 5 contains a discussion of the results, conclusions and a projection of future work with the model. We have also included appendices that detail the nondimensionalization and discretization of the differential equations.

2. The model

Our model describes conservation of mass, momentum, energy and species concentration for a two-component, fluid–solid system undergoing directional solidification. The model is two-dimensional and the equations are written in terms of volume-averaged quantities [27,50]. We assume that the fluid–solid system is contained within a Hele–Shaw cell and, hence, that conservation of momentum can be expressed within the mushy region *and* the open fluid region with Darcy’s law. In the pure solid region a fluid flux of zero is prescribed. Furthermore, as is usual for theoretical studies of mushy layers, we assume local (i.e. within each averaging volume) thermodynamic equilibrium everywhere over the domain [49]. With this assumption the local temperature, solid fraction and phase compositions are entirely determined by the local enthalpy, bulk composition and a statement of the binary phase diagram. This thermodynamical modeling approach is termed the Enthalpy Method and has been used in fluid dynamics problems with phase changes [2,38,8]. Within the Enthalpy Method, the equations describing conservation of energy and conservation of bulk composition apply over the whole domain.

The domain, shown in Fig. 2 has a height h and a Hele–Shaw gap-width d . The height is defined, in accord with experiments, as the distance between heat exchangers that impose the top and bottom temperature, T_{cold} and T_{warm} , respectively, and that are fixed in the laboratory reference frame. A uniform, constant downward velocity V transports solid and liquid through the computational domain and represents the translation of the Hele–Shaw cell through the heat exchangers in experiments [33]. The simulation is initiated with temperature T_i and concentration C_i within the interior of the domain. T_{cold} is typically below the eutectic temperature of the solution and hence solidification begins at the bottom boundary and progresses upward. We choose an initial concentration C_i that is on the NH_4Cl side of the eutectic, thus the mushy layer is composed of solid NH_4Cl crystals and a residual liquid that is fresher and less dense as a result of solidification. Variations in density enter the governing equations only in the buoyancy terms. Elsewhere, we assume that the fluid and solid densities are identical and constant. The effect of a density difference between fluid and solid has been previously considered and shown to have negligible effect on the dynamics [14,15]. The dimensional values of all parameters used in this model are given in Table 2.

Boundary conditions are chosen to be consistent with directional solidification experiments [33,34] and are shown in Fig. 2. The computational domain has impermeable side and bottom boundaries and a permeable top boundary. The latter allows chemically buoyant plumes to escape instead of polluting the interior of the domain. The top boundary is also no-slip (i.e. no tangential velocity), which is artificial with respect to experiments but useful because it helps to reduce lateral flow

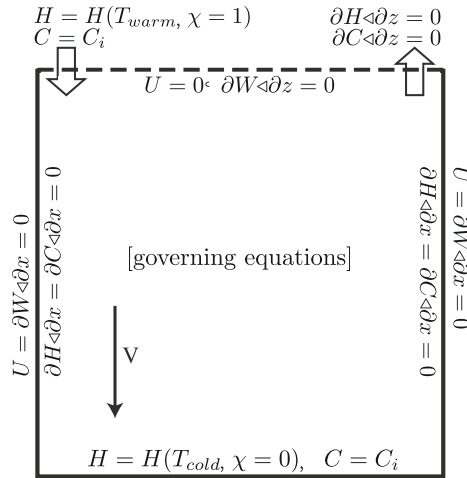


Fig. 2. A schematic diagram of the computational domain with boundary conditions. The temperature and porosity are fixed at the top and bottom of the domain by calculating their corresponding value of H using Eq. (1). On the top boundary, the direction of fluid flow determines the set of boundary conditions that are applied. The side boundaries are impermeable; reflection conditions on H and C enforce zero diffusion across them. A reflection condition on the vertical flux at the side boundaries is appropriate because Darcy flow need not satisfy a no-slip condition.

within the liquid region. Fixed temperatures are imposed at the top and bottom. The sides are thermally insulating. Along the top boundary, grid cells where fluid is flowing out of the domain use a reflection boundary condition on bulk composition; where fluid flows into the domain it does so with prescribed bulk composition.

The primary unknowns in the simulation are bulk enthalpy H bulk solute concentration C and the two-dimensional Darcy flux \mathbf{U} . Other variables (temperature, porosity, phase concentrations and permeability) are determined from the main variables using constitutive laws. Below we detail the partial differential equations and constitutive laws that govern the system and give an overview of our implementation of the numerical solution of these equations. The equations are solved in terms of nondimensional variables; Appendix A presents our choice of scales and resulting nondimensional equations.

2.1. Conservation of energy

The enthalpy (J m^{-3}) of a fixed volume of fluid and solid with porosity χ is given by

$$H = H_0 + \chi\rho L + \chi\rho c_{p,l}(T - T_e) + (1 - \chi)\rho c_{p,s}(T - T_e), \tag{1}$$

where H_0 represents the reference enthalpy of the solid at the eutectic temperature T_e , ρ is the density, L is the latent heat per kilogram of liquid and $c_{p,s}$ ($c_{p,l}$) is the specific heat of the solid (liquid). In what follows we take the reference enthalpy to be zero.

Energy is transported by translation of the containing cell, fluid advection, diffusion through the solid and the fluid, and diffusion out of the Hele-Shaw cell through its walls. The latter effect has been previously characterized [33] for the experimental apparatus used in Fig. 1. We adopt their parametrization and write conservation of energy as

$$\frac{D_V H}{Dt} + \mathbf{U} \cdot \nabla H = \nabla \cdot [\chi k_l + (1 - \chi)k_s] \nabla T - b(T - T_\infty), \tag{2}$$

where \mathbf{U} is the Darcy flux, equal to the porosity times the volume averaged microscopic velocity [27], k_l and k_s are the thermal diffusivity in the liquid and solid, T_∞ is the ambient temperature surrounding the modeled Hele-Shaw cell and b is an empirically determined parameter that quantifies the efficiency of thermal transfer with the ambient air [33]. The Lagrangian derivative is defined as

$$\frac{D_V}{Dt} = \frac{\partial}{\partial t} + V \frac{\partial}{\partial z}, \tag{3}$$

which accounts for transport due to the translation of the Hele-Shaw cell through the domain with velocity V .

2.2. Conservation of solute

The solute, NH_4Cl , is transported through the domain by translation of the containing cell, advection by the liquid and diffusion through the liquid. We can write the conservation of solute as

$$\frac{D_V C}{Dt} + \mathbf{U} \cdot \nabla C = \nabla \cdot \chi D_1 \nabla C, \tag{4}$$

where C is the bulk concentration (kg m^{-3}), C_l is the liquid concentration and D_l is the solute diffusivity in the liquid. The bulk concentration is defined as

$$C = \chi C_l + (1 - \chi) C_s. \tag{5}$$

2.3. Conservation of mass and momentum

Since the solid does not deform and we make the Boussinesq approximation, conservation of mass is written

$$\nabla \cdot \mathbf{U} = 0. \tag{6}$$

As described above, we use Darcy’s law throughout the domain to enforce conservation of momentum

$$\nabla p = \rho g [\alpha(T - T_e) + \beta(C - C_e)] \mathbf{k} - \frac{\eta}{\Pi} \mathbf{U}. \tag{7}$$

Here, p is the dynamic fluid pressure, g is the acceleration of gravity, α and β are the thermal and solutal expansivities ($\beta < 0$), T_e and C_e are the eutectic temperature and concentration, η is the fluid viscosity and Π is the permeability. The Darcy flux, \mathbf{U} , is taken in a frame moving with the translating Hele-Shaw cell. Taking the curl of Eq. (7) and rearranging gives

$$\frac{\rho g}{\eta} \left(\alpha \frac{\partial T}{\partial x} + \beta \frac{\partial C}{\partial x} \right) = \nabla \times \frac{\mathbf{U}}{\Pi}. \tag{8}$$

2.4. Constitutive equations

While the principle variables, H , C and \mathbf{U} , are constrained by the governing PDEs, constitutive laws are used to relate the values of these variables to other properties of the system.

2.4.1. The Enthalpy Method

Because we have assumed that the system is in local thermodynamic equilibrium everywhere in the domain, we can determine the local temperature, phase fraction and solute concentration in each phase from local values of the enthalpy and bulk composition [2,8,38]. To do so, however, requires a statement of the phase diagram in temperature–composition space. We follow previous authors in prescribing a phase diagram with a eutectic, a linear liquidus $T_l(C_l)$ and a constant partition coefficient $p_c = C_s/C_l$ describing the distribution of solute between the phases, as shown in Fig. 3. The liquidus is given by

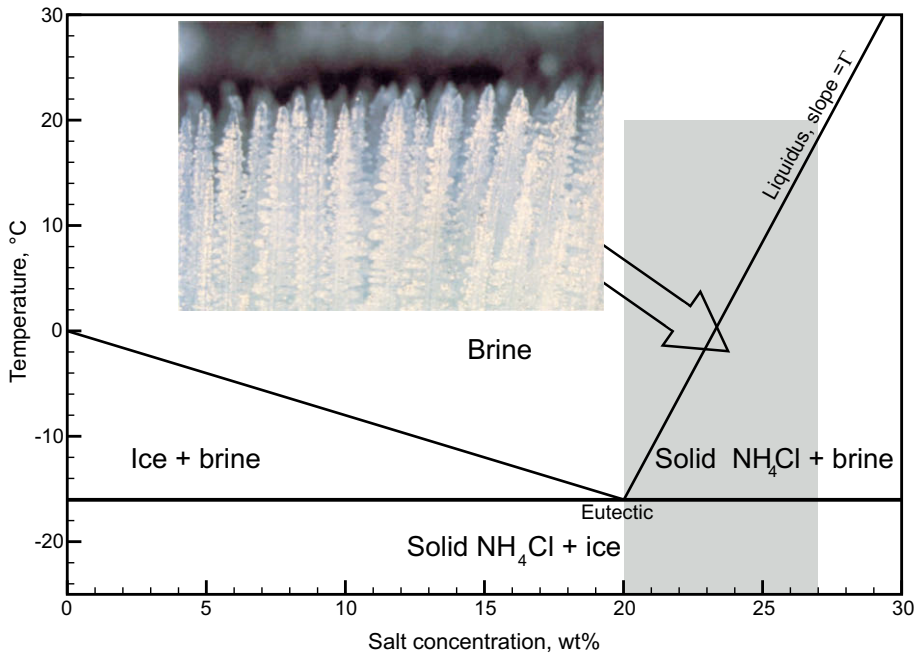


Fig. 3. A schematic phase diagram of the binary NH_4Cl -water system. The NH_4Cl solidus is not shown; it is defined by Eq. (10) and is, at most, $p_c C_e$ away from pure NH_4Cl . The gray region contains the conditions typically used in experiments on the solidification of NH_4Cl . The image shows the mush–liquid interface of a mushy layer made of NH_4Cl dendrites.

$$T_L(C_l) = T_e + \Gamma(C_l - C_e), \quad (9)$$

where Γ is the slope of the liquidus. The solidus is given in terms of the solid concentration as

$$T_S(C_s) = \max \left[T_e, T_e + \frac{\Gamma}{p_c} (C_s - p_c C_e) \right]. \quad (10)$$

To calculate the thermo-chemical state at a grid-cell, we first need to determine the region of the phase diagram corresponding to local values of H and C . Using information from the phase diagram and Eq. (1) we can determine, for given C , (a) the energy H_S at which the cell reaches the eutectic from below but is entirely solid, (b) the energy H_E at which it leaves the eutectic for the liquidus and (c) the energy H_L at which it leaves the liquidus and is entirely molten. H_S , H_E , and H_L are determined using Eq. (1) with (χ, T) equal to $(0, T_S(C))$, (χ_E, T_e) , and $(1, T_L(C))$, respectively. The porosity χ_E is calculated using Eq. (5) with $C_l = C_e$ and using the definition of the partition coefficient as

$$\chi_E = \frac{C - p_c C_e}{C_e - p_c C_e}. \quad (11)$$

For an enthalpy below the solidus ($H \leq H_S$) the local system is entirely solid so $\chi = 0$, $T = H/(\rho c_{p,s})$, $C_s = C$ and C_l is arbitrary but taken as equal to C_e . Similarly, when the local enthalpy is above the liquidus, ($H \geq H_L$), $\chi = 1$, $T = (H - \rho L)/(\rho c_{p,l})$, $C_l = C$ and C_s is arbitrary but taken as $p_c C$. There are two other, more complicated cases: the local system is at the eutectic when $H_S < H \leq H_E$, or the local system is on the liquidus for $H_E < H < H_L$. The means for calculating porosity, temperature and phase compositions for these two cases are summarized, in nondimensional form, in Table A.2.

2.4.2. Permeability

Permeability is typically modeled as varying with porosity from zero at $\chi = 0$ to infinity at $\chi = 1$. In a Hele-Shaw cell the permeability of the system is limited by the permeability of the cell itself, $d^2/12$ [7]. To impose this limit we adopt a dimensional permeability of the form

$$\Pi(\chi) = \left(\frac{12}{d^2} + \frac{1}{\Pi_\chi} \right)^{-1}, \quad (12)$$

where Π_χ is a function that parametrizes the variation of permeability with porosity. The total permeability is thus the harmonic mean of the cell permeability and the mush permeability. This mean is roughly equivalent to taking the minimum of the two arguments but has the advantage of being continuous and differentiable.

The canonical choice for Π_χ is the Kozeny–Carmen relationship,

$$\Pi_\chi = \frac{\Pi_0 \chi^3}{(1 - \chi)^2}, \quad (13)$$

where Π_0 is a factor related to the mean pore diameter [7]. As shown in Fig. 4, this function varies significantly over a range of porosities near $\chi = 1$. An alternative form representing flow along parallel cylinders, with a smaller variation in permeability near $\chi = 1$, was adopted by Tait and Jaupart [20,42]. We have simplified their relation slightly but retain the logarithmic singularity at $\chi = 1$

$$\Pi_\chi = -\Pi_0 \chi^2 \ln(1 - \chi). \quad (14)$$

As shown in Fig. 4, this function behaves as χ^3 for porosity approaching zero, similar to Kozeny–Carmen.

2.5. Implementation of numerical solution

The nondimensional governing equations are discretized on a staggered Cartesian mesh using a finite volume approach and uniform grid spacing. Fluid fluxes are evaluated on the borders between grid cells while other variables are evaluated at cell centers [23] making the discrete equations flux-conservative. Diffusion terms are discretized with standard second-order finite difference stencils. Time is discretized using a Crank–Nicolson scheme (i.e. semi-implicit; the values of terms in Eqs. (A.1) and (A.2) are calculated using the mean of the fields at the current and next step) for second-order accuracy. Lagrangian time derivatives are discretized by the semi-Lagrangian advection method [40,39]. The time-step size is determined according to a Courant–Friedrichs–Lewy (CFL) condition on the maximum velocity at the previous time-step. All Enthalpy Method variables are updated simultaneously with the enthalpy and bulk composition. The discrete equations are presented in Appendix B.

For accelerated solver convergence and efficiency, we divide the set of discrete equations in two, beginning each time-step by solving for a predicted enthalpy and bulk composition at discrete time $n + 1$ using Eqs. (A.1) and (A.2) and taking values of the flux from the solution at time n . This prediction is then used to solve for the flux at $n + 1$ with Eqs. (A.3) and (A.4). We iterate this sequence, updating the enthalpy and bulk composition at time $n + 1$ using the mean of the flux averaged between times n and $n + 1$, then updating the flux at $n + 1$ using the newly calculated thermodynamic fields. Each iteration of this sequence improves the accuracy of the solution. In practice we find that for a CFL number of around unity, a

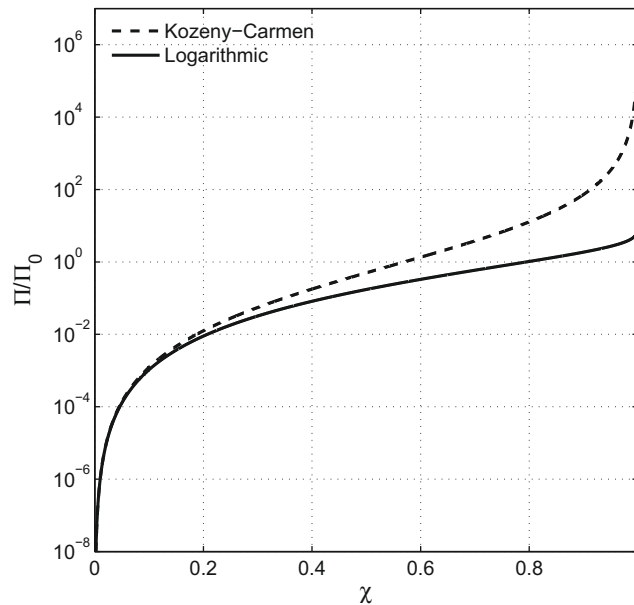


Fig. 4. Variation in nondimensional permeability with porosity. For a given value of Π_0 and a representative porosity of 0.9, Kozeny–Carmen (Eq. (13)) produces a permeability that is about two orders of magnitude larger than the logarithmic permeability function (Eq. (14)). We thus expect similar results from simulations with different permeability function where the values of Π_0 differ by about two orders of magnitude.

single iteration is sufficient to achieve an accuracy for the entire system of equations that is consistent with the accuracy of each of the two iterated solution blocks.

Eqs. (A.1) and (A.2) have nonlinearities arising from the Enthalpy Method and from the nonconstant diffusivity. Even with the flux \mathbf{U} fixed, the corresponding discrete equations require the use of a nonlinear solver. The discrete equations corresponding to (A.3) and (A.4), on the other hand, are linear for fixed permeability. Although we fix the permeability while we update the flux, for convenience and consistency we adopt the same solution strategy as for the update of enthalpy and composition (see below). Special care must be taken when the discrete momentum equation is evaluated on a patch of grid where the permeability is zero—see Appendix B for details.

The two discrete solutions are determined using a Newton–Krylov–Schwartz method [12] that is provided by the Portable Extensible Toolkit for Scientific Computation (PETSc) [5,4]. This method is suited for sparse sets of coupled, nonlinear equations in N dimensions on a domain that is decomposed into regions with boundaries in $N - 1$ dimensions. The method begins with an initial guess \tilde{x} that is iteratively updated with a correction δx , determined by solving the linear system $J\delta x = r$, where r is a vector representing the residuals of the discrete equations and J is the Jacobian matrix given by $\partial r_i / \partial \tilde{x}_j$ (Jacobian-free variants of this method are also possible, e.g. [25]). The solution to this linear system is preconditioned with an Incomplete LU (ILU) factorization and solved using the Generalized Minimum Residual (GMRES) method [35,18]. Newton iteration continues until the norm of the residual vector is below a user-specified tolerance. For mushy layer simulations we set this tolerance to 10^{-7} or less.

PETSc provides a variety of solver methods with a unified, relatively simple interface; for each set of nonlinear equations to be solved, the user must create a subroutine for calculating the discrete residual at each grid point [23]. The Jacobian can be generated automatically by PETSc using finite differences or specified via a user-provided subroutine (we opt for the former). Furthermore, PETSc’s data structures and methods are inherently parallel and scalable [6,23]; our mushy layer simulations are typically run on 4–6 processors.

3. Validation

Validation of the code requires a demonstration that the numerical solution is an accurate representation of the exact solution at an achievable grid resolution and that the numerical solutions converges to the exact solution with increasing grid resolution. As usual, there is no exact solution for the full problem that is being simulated. There are, however, two test cases that provide acceptable benchmarks for the two core components of the code. The first is an analytic solution for the steady-state profile of a mushy layer under directional solidification with no fluid flow [21,19,46]. Comparison of this solution with numerical results for prescribed zero fluid flux validates our implementation of the Enthalpy Method. The second benchmark involves comparison with a consensus of previous numerical simulations [28]. These simulations model steady-state convection in a 2D box containing a fixed porous medium of unit permeability with fixed temperature on the left and

right walls and zero heat flux on the top and bottom. Comparison of these consensus results with our own results for the same model validates our numerical treatment of Darcy's equation and advection and diffusion of heat.

There are important components of our simulations that are not validated by these two tests, including our treatment of the advection of solute and our success in modeling flow through a porous medium that has orders of magnitude spatial variation in permeability. Qualitative comparison of results (see below) with experiments [34] and other models [36,16], in addition to past work on different simulations with similar discretization [1,23], gives confidence that our numerical implementation of the model achieves reasonable accuracy, overall.

3.1. Solidification without fluid flow

Worster [46] summarizes the analytical solution for mushy layer height and porosity as well as temperature and liquid solute concentration [21,19]. The domain is a 1D profile through a semi-infinite half space with an imposed directional solidification rate V . The eutectic temperature is imposed at $z = 0$ and the far-field temperature and concentration are specified. There is no fluid motion and the heat capacities and thermal conductivities are taken as equal in the liquid and solid. See [46] for further details.

The numerical simulations are based on a reduced model given in nondimensional terms by

$$D_V \mathcal{H} / Dt = \partial_{zz} \theta, \quad (15)$$

$$D_V \Theta / Dt = Le^{-1} \partial_z \chi \partial_z \Theta_1. \quad (16)$$

\mathcal{H} , Θ and θ are the nondimensional enthalpy, bulk concentration and temperature, respectively, and Le is the Lewis number. Details of the nondimensionalization are given in Appendix A. Parameter values are assigned to be compatible with the analytical solution (e.g. $k_l = k_s$, $c_{p,l} = c_{p,s}$).

Fig. 5 shows a comparison between profiles obtained from the numerical solution and from analysis (the curves are indistinguishable).

3.2. Convection in a fixed porous medium

Buoyancy-driven fluid flow is the second key component of our simulations. To benchmark our ability to accurately model flow and advection of heat we simulate convection in a fixed, uniform permeable medium with no phase change. The domain is a unit square with imposed temperature on the left (warm) and right (cool) boundaries and no heat flux through the top and bottom. For consistency with previous work, we include a viscous dissipation term in the momentum equation and require that fluid on the boundaries has zero velocity. The thermal Rayleigh number and Darcy number are the only dimensionless parameters. The details of this benchmark have been previously discussed [28,26,31].

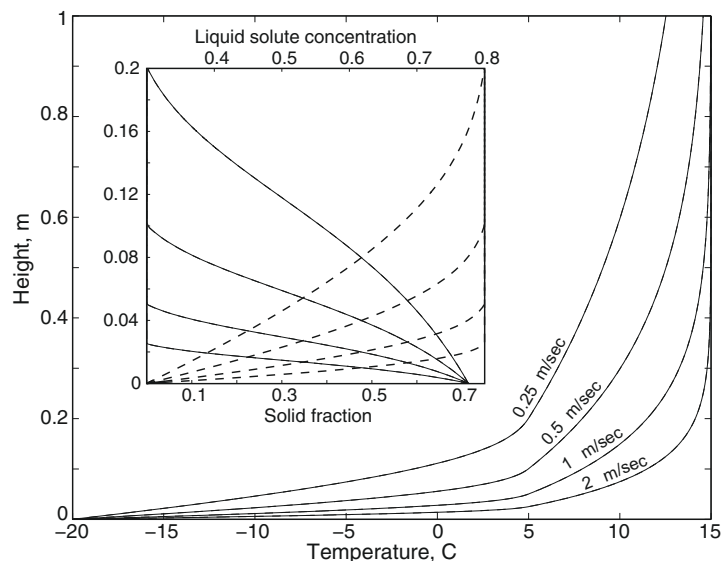


Fig. 5. Steady-state profiles of directional solidification of a binary alloy in simulations compared with an analytical solution [21,19,46]. The difference between analytical and numerical curves is smaller than the line thickness and therefore not visible. In the inset panel, dashed curves represent liquid solute concentration. The curves within each set are distinguished by the Hele-Shaw cell translation rate V , which varies in factors of two from $0.25 \mu\text{m/s}$ for the uppermost curves, to $2 \mu\text{m/s}$ for the lowermost curves. There is no fluid motion; the kinks in the temperature curves are the result of latent heat release at the top of the mushy layer. Nondimensional parameters used for these calculations (see Appendix A) are $S = 5.7$, $\mathcal{C} = 1.4$, $K = 1$, $c_p = 1$, and $Le \rightarrow \infty$.

Table 1

A comparison of the mean Nusselt number at different values of the Rayleigh and Darcy numbers

Da	Ra_T	This study	Ref. [28]	Ref. [26]	Ref. [31]
10^{-6}	10^7	1.08	1.08	1.07	1.08
	10^8	3.10	3.08	3.06	3.00
	10^9	13.4	13.2	13.2	12.3
10^{-4}	10^5	1.07	1.07	1.06	–
	10^6	2.86	2.85	2.84	–
	10^7	10.3	10.3	10.3	–
10^{-2}	10^3	1.02	1.02	1.02	1.02
	10^4	1.71	1.71	1.70	1.71
	10^5	4.33	4.26	4.26	4.26

Within the domain the permeability, porosity, fluid concentration, thermal conductivity and specific heat are all unity. The simulations were performed on a uniform mesh with 242×242 cells.

We run the simulation until a steady-state is reached, defined as

$$\max(|\theta^{n+1} - \theta^n|) / \Delta t_n < 10^{-3}, \quad (17)$$

where n indexes successive time-steps and Δt_n is the length of the time-step. We then calculate the Nusselt number, $\partial\theta/\partial x$, averaged over the left and right boundaries. A comparison with results from previous studies is given in Table 1 and the agreement signifies valid implementation of the conservation of mass, momentum and thermal energy equations.

4. Simulations of directional solidification

We now consider solutions of the full governing equations. In Section 4.1, we report on an ensemble of simulations with parameter values that match directional solidification experiments on aqueous ammonium chloride (including the Hele-Shaw gap width of 5 mm) [34]. The domain is 6 cm in height, as in experiments, but has a width that is one half the 12 cm width of the experimental apparatus. We vary the magnitude and functional form of the permeability over the ensemble and study the consequences. In Section 4.2, we consider a simulation that uses parameters modified from their natural values to suppress the boundary layer mode of instability. In this case we force the mushy layer to go unstable by the mushy layer mode as described in Ref. [47].

4.1. Solidification of aqueous NH_4Cl

The relationship between permeability and porosity in crystalline mushy layers grown from standard materials is not well known; other parameters have been accurately measured and reported in the literature. We performed an ensemble of simulations in which we varied the permeability law (between Eqs. (13) and (14)) and the permeability constant Π_0 . Parameters C_i , V , T_{warm} and T_{cold} are as for the experiment shown in Fig. 1 (and also for $V = 3 \mu\text{m/s}$). Other parameters corresponding to solidification of NH_4Cl from an aqueous solution are given in Table 2.

For a given permeability function, changing the constant Π_0 affects the thickness of the mushy layer as a function of time (Fig. 7), as well as the number and type of perturbations to the mush–liquid interface. In simulations with small values of Π_0

Table 2Properties of the NH_4Cl –water system (on the side of the eutectic where NH_4Cl is the crystallizing phase) and of the directional solidification apparatus

Parameter	Value	Units	Comment
η	1.4×10^{-3}	Pa s	Viscosity at 20 °C
k_l	0.54	$\text{W m}^{-1} \text{K}^{-1}$	Liquid heat conductivity
k_s	2.2	$\text{W m}^{-1} \text{K}^{-1}$	Solid heat conductivity
$c_{p,l}$	3.5×10^3	$\text{J kg}^{-1} \text{K}^{-1}$	Liquid specific heat
$c_{p,s}$	1.5×10^3	$\text{J kg}^{-1} \text{K}^{-1}$	Solid specific heat
ρ	1050	kg m^{-3}	Density of the liquid
L	2.76×10^5	J kg^{-1}	Latent heat of dissolution
α	2.1×10^{-4}	K^{-1}	Thermal expansivity
β	–0.30	(wt. frac.) ^{–1}	Solutal expansivity
T_e	–16	°C	Eutectic temperature with water
C_e	0.8	wt. frac.	Water concentration at eutectic
Γ	471.4	°C (wt. frac.) ^{–1}	Liquidus slope
p_s	10^{-5}		Water distribution coefficient
b	1600	$\text{J m}^{-3} \text{s}^{-1} \text{°C}^{-1}$	Hele-Shaw cell cooling coefficient [33]

The distribution coefficient, p_s , that describes the water content of solid NH_4Cl is taken as nonzero for stability of the numerical method.

and hence low permeability (less than about 5×10^{-14} for Kozeny–Carmen, 10^{-10} for logarithmic permeability), convection occurs in the boundary layer mode [47] and corrugations form on the mush–liquid interface but do not grow into chimneys. Individual corrugations are transient; together they produce a small decrease in the thickness of the mushy layer, which reaches steady-state in about 90 min of simulated time.

For larger values of Π_0 , boundary-layer-mode corrugations on the mush–liquid interface activate convection in the mush below. Fresh fluid upwells through the mushy layer and is vented from a subset of the corrugations. Reactions between the upwelling fluid and the porous matrix lead to dissolution of mush beneath the corrugations and to their downward extension to form chimneys. Fig. 6 shows a time series of permeability maps from a simulation that developed chimneys; in this case, the Kozeny–Carmen relation (13) was used to calculate permeability with $\Pi_0 = 10^{-12}$. The presence of chimneys reduces the thickness of the mushy layer relative to chimney-free cases; the number of chimneys evolves with time (and with mushy layer thickness). Chimney spacing for the ensemble of simulations is discussed below and shown in Fig. 8.

In cases where chimneys occur, the onset of convection in the mushy layer and hence growth of corrugations into chimneys typically occurs within the first few minutes of simulated time. Moreover, for larger values of Π_0 , initial corrugations cross the nascent, thin mushy layer and are thus indistinguishable from chimneys. The curves describing mushy layer height for cases of early chimney onset, shown in Fig. 7, are monotonically increasing with time (small oscillations are a known artifact of the Enthalpy Method related to finite jumps of the eutectic boundary across grid cells [2]). There are several curves in Fig. 7, however, which are not monotonically increasing. In the simulations corresponding to these curves, the mushy layer grows for at least 10 min before corrugations extend downwards into the mush to become chimneys. This late onset

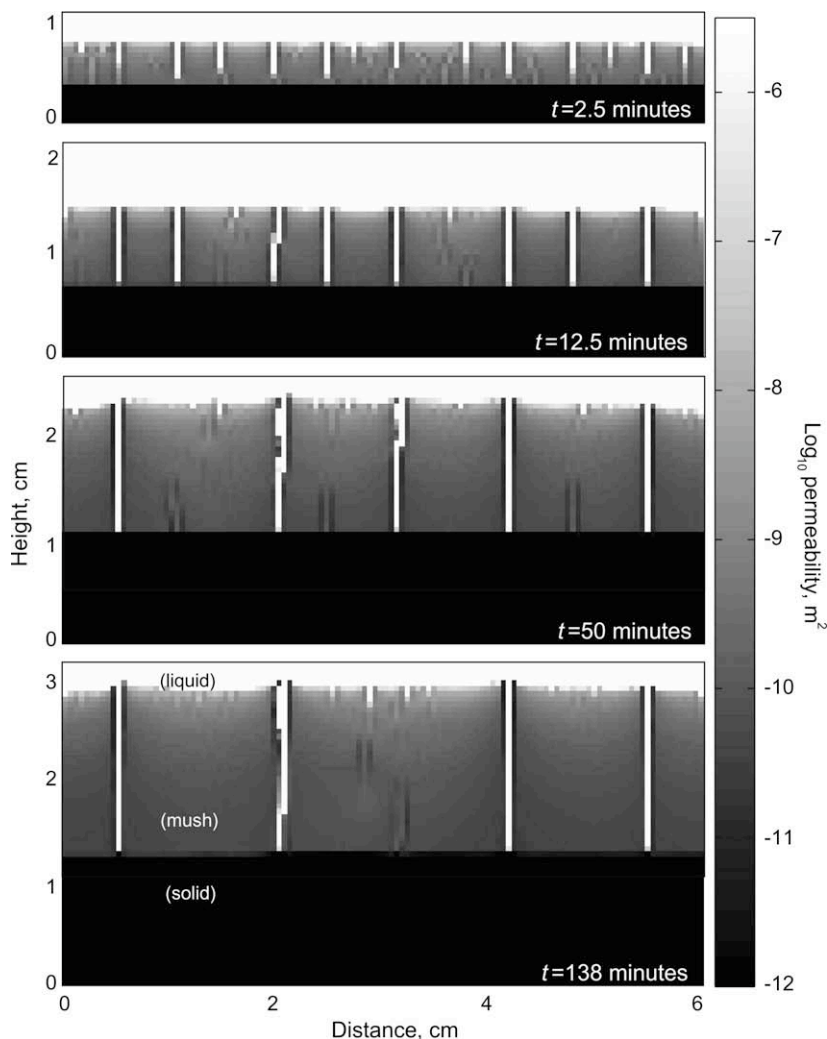


Fig. 6. Four permeability maps from a simulation of directional solidification of aqueous NH_4Cl . The gray-scale corresponds to the base-10 logarithm of permeability in m^2 . For this simulation, permeability was calculated using the Kozeny–Carmen relation (13) with $\Pi_0 = 10^{-12}$. Dimensional parameters are as given in Table 2. The grid spacing is 1/2 mm in both directions. An assigned CFL number of 1.5 for this simulation yielded time-steps of ~ 1 s of model time early in the simulation before the onset of vigorous convection, and ~ 0.1 s late in the simulation.

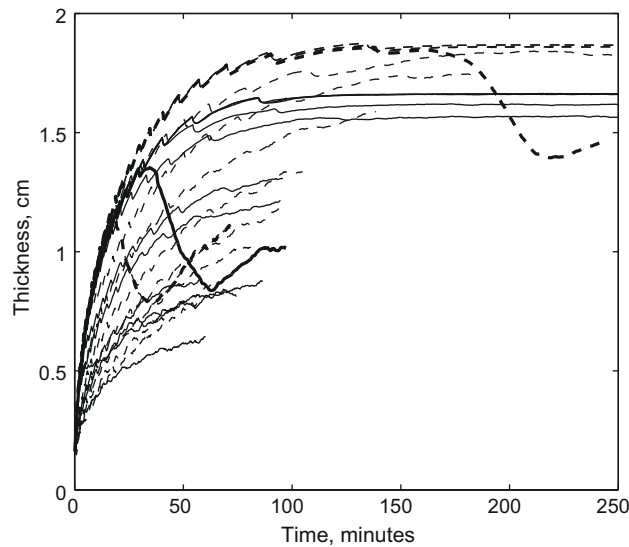


Fig. 7. Mushy layer thickness as a function of time for an ensemble of simulations with different values of Π_0 . The jaggedness of the curves is the result of a known artifact of the Enthalpy Method in which the location of the eutectic boundary undergoes finite jumps between grid cells [2]. Dashed lines represent simulations with $V = 1 \mu\text{m/yr}$, solid lines represent simulations with $V = 3 \mu\text{m/yr}$. Simulations with delayed onset of chimney formation and oscillatory mushy layer thickness are highlighted with heavy lines. Most of the simulations were run for 40 h on five processors; simulations without strong chimney convection ran with larger time-steps and hence reached larger simulated times.

of chimney formation corresponds to a decrease in mushy layer thickness that slows with time and is followed by a second period of mushy layer growth.

Simulations that do not produce chimneys reach a steady state mushy layer height. For a given computational effort, they traverse a greater period of simulated time because their weak convection allows longer time-steps. Simulations with chimneys, on the other hand, have strong convection and hence smaller time-steps. For the same computational effort, they traverse smaller simulated times, as is evident in Fig. 7. Although they do not, in general, reach a steady-state mushy layer height over this time interval, they do achieve sufficiently small rates of growth that the number and spacing of chimneys is in equilibrium with the height. In simulations with monotonically increasing mushy layer thickness, the number of chimneys decreases monotonically.

Fig. 8 shows the ratio of chimney spacing to mushy layer height plotted against the value of Π_0 from simulations. The data were taken from the last time-step of each simulation that produced chimneys and hence represents its most mature state. Simulations at different Hele-Shaw cell translation rates V show no apparent difference in chimney spacing to mushy layer height ratio. This is not surprising given that both spacing and height are expected to vary with the thermal length-scale, κ/V [47]. For both permeability laws, at smaller Π_0 the chimney spacing is approximately equal to twice the mushy layer height, consistent with predictions from linear stability analysis [47]. Such simulations have Rayleigh numbers that are only slightly above the critical Rayleigh number for the onset of convection in the mush. The Rayleigh number increases with Π_0 , and simulations summarized in Fig. 8 show that this leads to closer spacing of chimneys at a given mushy layer height.

Another interesting feature discernible in Fig. 8 is the *difference* between trends for the two permeability laws. Chimney convection under Kozeny–Carmen occurs at a minimum value of Π_0 that is about four orders of magnitude smaller than the minimum for Logarithmic permeability. However, the difference in permeability between these two laws for a fixed value of Π_0 and a porosity $\chi = 0.9$, representative of the bottom of the mushy layer, is only about 100 (see Fig. 4). This suggests that chimney formation is more sensitive to the permeability at the top of the mushy layer, even though chimneys penetrate to the base of the mushy layer. Such behavior is to be expected if the boundary layer mode of instability is responsible for initiating the process of chimney formation.

4.2. The mushy layer mode

The simulations described in the previous section use parameters that are constrained, as much as possible, by the physical properties of aqueous ammonium chloride and by the properties of an experimental apparatus in use at the University of Cambridge [33]. In these simulations, the boundary layer mode is always first to go unstable and chimneys form by growth of perturbations to the mush–liquid interface. By changing parameter values, it is possible to suppress the boundary layer mode of convection so that the system goes unstable by the mushy layer mode. There is some indication that the mushy layer mode of instability is active in fixed-chill experiments where the temperature contrast between the cold plate and the ambient fluid is slowly increased from zero [41,42].

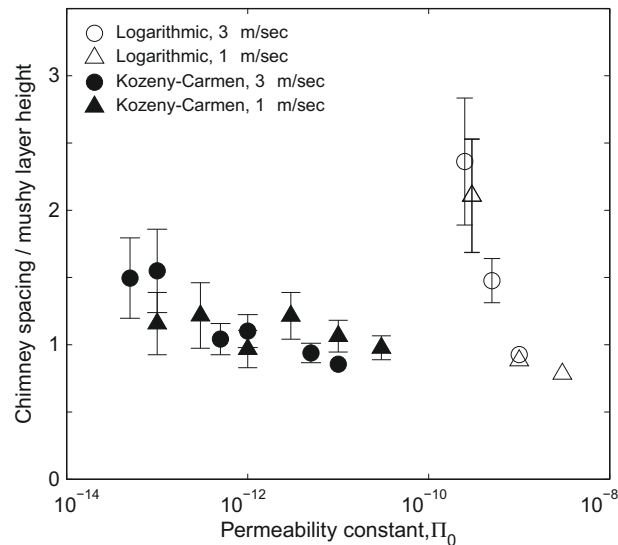


Fig. 8. The ratio of chimney spacing to mushy layer height as a function of Π_0 for an ensemble of simulations with $C_1 = 25$ wt% NH_4Cl (parameters as in Table 2, top and bottom temperatures as in Fig. 1). Symbol shape denotes the translation rate of the Hele-Shaw cell V ; symbol fill denotes the permeability law used in the simulation, Eq. (13) or (14). Error bars show the range of chimney spacing within the simulation; they are not added to points where the range is smaller than the size of the symbol. Simulations with zero chimneys have an infinite y -coordinate on this plot. Such results were obtained for Π_0 just below the smallest plotted values in each trend. See the main text for a description of trends.

The boundary layer mode is driven by the presence of a mobile, buoyantly unstable compositional boundary layer at the mush–liquid interface. It results from solidification of the mush and diffusive transport of solute downward into fresher fluid below. Reduction of the solutal diffusivity therefore diminishes the driving force for boundary layer mode convection. This is not sufficient, however, because the boundary layer mode can be initiated by buoyant rise of fluid from just below the mush–liquid interface, where the solid fraction is low and the permeability is high. Full suppression can be achieved by reducing the mobility of the fluid outside the mushy layer relative to the fluid within the mushy layer, i.e. increasing the Darcy number, $Da = 12\Pi_0/d^2$.

Fig. 9 shows the development of the mushy layer mode in a simulation with parameters modified from experimental constraints. In this mode of instability, the buoyancy of interstitial fluid within the mushy layer drives convection at a wavelength that is about two times the thickness of the mushy layer [47]. Upwellings are initially broad and symmetric with downwellings. The flow modifies the permeability via dissolution, associated with upwelling, and precipitation, associated with downwelling. With time, upwelling flow is focused into zero-solid-fraction chimneys of decreasing width.

Fig. 10 shows material streamlines and isotherms overlaid on the permeability structure of the mush. Material streamlines denote the instantaneous velocity field in the laboratory reference frame, they are not fluid particle trajectories. Nonetheless, they indicate the presence of a stagnation point below the chimney. The black curve in this figure is the line on which $\mathbf{q} \cdot \nabla T = \mathbf{q} \cdot \nabla C_1 = 0$ ($\mathbf{q} = \mathbf{U} - V\mathbf{k}$ is the material flux in the laboratory reference frame), or, equivalently, the line that connects points of tangency between the streamlines and isotherms. The lowest point on this curve is where flow stagnates. When the mushy layer is in steady-state, this line marks the boundary between the chimney and the mush [37]. In Fig. 10, however, the dashed curve encloses mush below the chimney, indicating that fluid is upwelling across isotherms in this region, dissolving crystals of the mush and causing the chimney to extend downward. At the same time, precipitation of mush is occurring within the walls of the chimney, narrowing its width and leading to the low permeability flanks that appear as dark vertical bands in Fig. 10.

Note the flanges or “corona” at the mush–liquid interface where the chimney vents its plume. These are formed by the chilling effect of diffusion of heat into the plume; solute-rich fluid surrounding the plume is cooled and precipitates crystals. The coronas around plumes in the experiment shown in Fig. 1 are visible but small compared with those predicted by the mushy layer mode simulation. In simulations, the size of the corona seems to correlate with the flux from the chimney. The chimneys shown in Fig. 6 have a relatively small flux and hence do not develop substantial coronas.

5. Discussion

Above we have described a theoretical/computational approach to modeling directional solidification, thermochemical convection and chimney formation in a Hele-Shaw cell. Using benchmark calculations, we have demonstrated the accuracy of the code in handling thermodynamic and fluid mechanical processes. Simulations of mushy layer formation and instability show that our code is capable of stably integrating the governing equations over hours of model time at high grid resolution. The results of these simulations are qualitatively consistent with experiments and with prior theory.

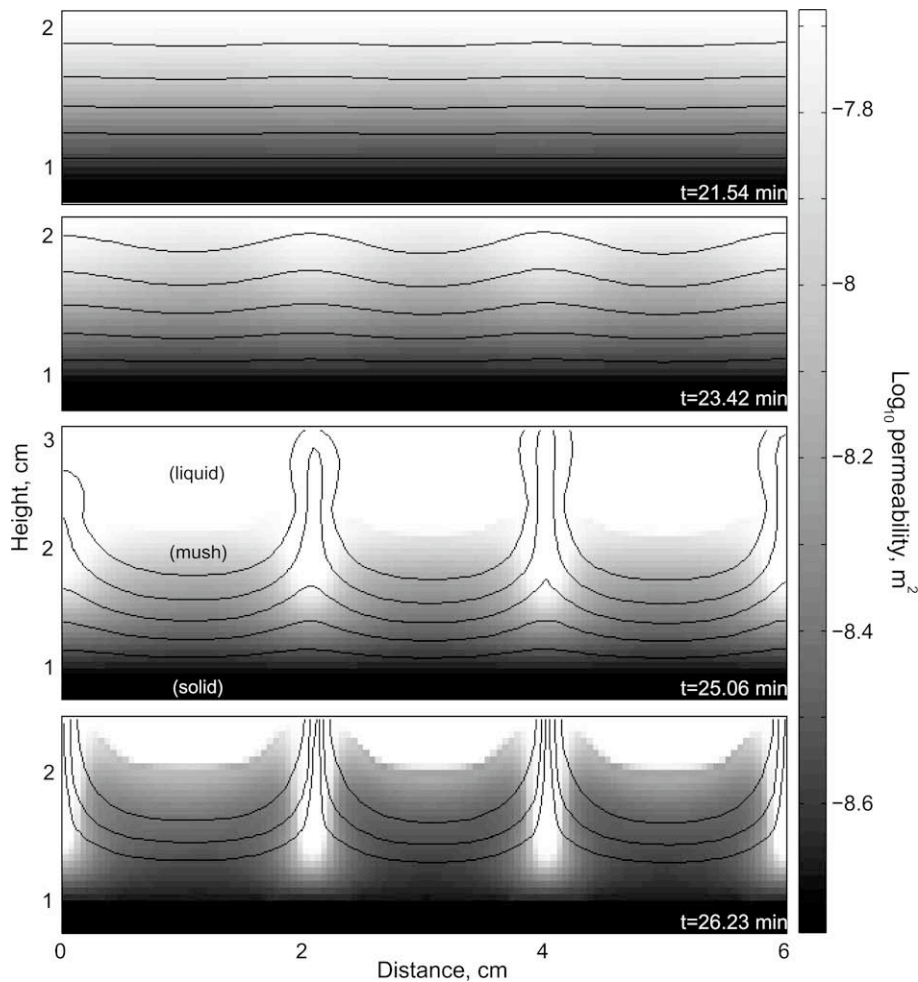


Fig. 9. A time series of simulation results showing the mushy layer mode of instability. The gray-scale denotes the logarithm of the permeability and contours represent lines of constant solute concentration in the fluid. This simulation uses Kozeny–Carmen permeability with $\Pi_0 = 10^{-11}$. The Darcy number is increased by a factor of 1000 over the simulation shown in Fig. 6. Note that the mushy layer is laterally uniform for more than 20 min before the instability occurs. Chimney width continues to decrease beyond the final image in this time series and stops when it has reached the grid spacing, which is 0.5 mm in this case.

Irrespective of the resolution of the computational grid or the primary instability mechanism, we find that simulated chimneys evolve to a width of one grid cell. This is unfortunate because it means that variations of flow across the chimney are not resolved, and that spurious numerical diffusion is likely to be playing a role in the simulations. This diffusion may artificially reduce convective vigor, however we have not shown this to be the case. In the governing equations solved here, we have neglected viscous shear stresses within the fluid. Experiments have shown that chimney width increases with fluid viscosity [42]. It is possible that the inclusion of shear stresses in our model would set a length-scale for the width of chimneys that is independent of grid spacing. This will be explored in future work.

To create a computational model of acceptable complexity and computational cost, we made two important simplifying assumptions. First, we assumed local thermodynamic equilibrium throughout the domain in order that we could apply the Enthalpy Method, and thus avoid the need to apply boundary conditions on internal, dynamic boundaries. Chemical kinetics may play a role in mushy layer evolution under some conditions; this is a subject we leave for future consideration. We also assume that the Hele–Shaw cell approximation of Darcy flow between parallel plates is valid for the directional solidification experiments that motivated our model, such as that shown in Fig. 1. This allows for an important control on plume ascent rates in the open fluid region of the domain, and hence a control on the minimum time-step size. Preliminary model development using a Darcy–Brinkman approach (after Ref. [28]) indicated that buoyant plumes restrained only by viscous stresses have large flow velocities; in simulations, this led to steps in model time of much less than one second, too small given the computational effort needed per time-step and the targeted interval of model time.

Besides the convenience of the Hele–Shaw approximation, there is the question of whether it is consistent with directional solidification experiments. The directional solidification apparatus at Cambridge has a gap of 5 mm between the glass

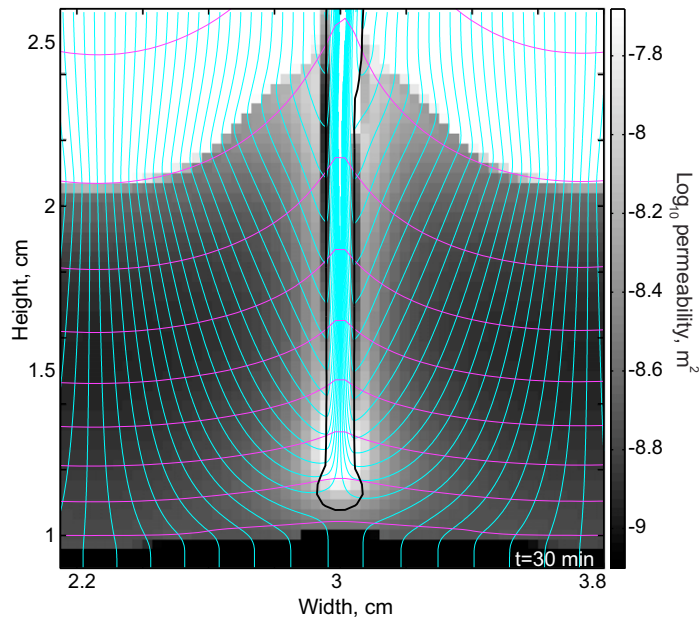


Fig. 10. Material streamlines and temperature contours superimposed on the permeability structure of the mushy layer. This simulation has a smaller grid spacing (0.3 mm) than the simulation shown in Fig. 9 but is otherwise identical. The black curve joins points where streamlines are tangent to temperature contours. At steady-state, this curve traces the chimney wall [37]. Within the chimney the solid fraction is zero. At this stage in the simulation, the chimney is still growing downward into the mush. It is becoming narrower due to crystallization along its walls. With time, crystallization leads to a low-permeability lining around the chimney, as shown in Fig. 6. This yields convection with a diminished depth of penetration and vigor.

plates that form the cell, larger than the 0.8–3.5 mm gap adopted in experimental analogues of flow in aquifers [7]. In directional solidification experiments on aqueous NH_4Cl , chimneys and their associated plumes do not span the entire 5 mm width of the cell. This is evident in a close inspection of Fig. 1: the visible chimneys are those that open onto the front panel of glass. There are others, discernible by their coronas, that open onto the back panel. The emitted plumes, likewise, do not span the width of the cell.

Despite this discrepancy, we feel that use of the Hele-Shaw cell approximation is justified by our focus on the evolution of the mushy layer, where the dynamics are dominantly controlled by the mush permeability. The form and ascent rate of plumes outside the mush are of no inherent interest for this work. Our study of the mushy layer mode of instability shows that an order of magnitude change in the Hele-Shaw gap width is needed to suppress the boundary layer mode and drastically change the system behavior. This indicates that the Darcy drag imposed by the cell width alone is not limiting the behavior of the system in the simulations of Section 4.1.

The simulations in Section 4.1 indicate that for conditions of directional solidification experiments on NH_4Cl (Fig. 1 and Refs. [34,45]), chimneys develop as a consequence of the nonlinear evolution of corrugations on the mush–liquid interface. These corrugations arise through the boundary layer mode of convective instability; their spacing is much smaller than the spacing of chimneys that develop when a subset of the corrugations grow downward into the mush. This behavior is qualitatively the same for the two different porosity–permeability relations used in this work (there are quantitative differences in chimney spacing, however). When the permeability of the mush is taken to be very high, the mushy layer remains thin and it is impossible to distinguish between interface corrugations and chimneys; otherwise, chimneys are considered to be zero-solid-fraction channels that extend through more than one third of the mushy layer’s depth. For low permeabilities, delayed onset of chimney formation leads to growth of the mushy layer to a significant height before chimneys develop from corrugations. This delay is reminiscent of the mushy layer mode of instability.

The mushy layer mode, however, has a very different pattern of disturbance to the porosity field. It appears, as predicted by linear stability analysis, with a long wavelength perturbation to the liquid concentration and the porosity. Upwelling fluid creates broad zones of zero-solid-fraction that vent buoyant plumes. With time, these broad vents narrow and extend downward to become chimneys. In regions between the chimneys, descending flows cool and precipitate solids. This leads to a decrease in convective vigor and an increase in mushy layer height and mean solid fraction.

The work described above exposes some of the basic features of numerical simulations of directional solidification. There are, however, many questions that have not been addressed here. Three general directions for further research with numerical simulations appear relevant: first, quantitative comparisons between simulations and experiments in terms of stability criteria, mushy layer height, and the spacing of chimneys will help to assess the physical assumptions of the present model and may help to constrain mush permeability. Secondly, exploration of the parameter space associated with linear stability calculations will refine our understanding of the evolution of convective instabilities into nonlinear regimes. This will help to

bridge the gap between stability analysis and steady-state theory of convection with chimneys. Finally, simulations can be calibrated to the NaCl–water system to model the formation of a mushy layer beneath sea ice. Such models could investigate the timing and magnitude of fluxes of cold, saline fluid off the ice and into the “ocean” below. All of these studies will have their basis, however, in the computational approach described here.

Acknowledgments

Thanks to M. Knepley, B. Smith, and S. Balay at Argonne National Laboratory for PETSc support and to Argonne’s Laboratory Computing Resource Center for use of the Jazz cluster. Two anonymous reviewers helped to improve the manuscript. Funding for R. Katz provided by the US National Science Foundation under the International Research Fellowship Program, Grant 0602101, and by the Research Councils UK under an Academic Fellowship.

Appendix A. Nondimensionalization

Using scalings and nondimensional parameters defined in Table A.1, we can write down a system of four dimensionless governing equations

$$D_V \mathcal{H} / Dt + \mathbf{U} \cdot \nabla \theta = \nabla \cdot [\chi + (1 - \chi)k] \nabla \theta - \mathcal{B}(\theta - \theta_\infty), \tag{A.1}$$

$$D_V \Theta / Dt + \mathbf{U} \cdot \nabla \Theta_1 = Le^{-1} \nabla \cdot \chi \nabla \Theta_1, \tag{A.2}$$

$$\nabla \times (\mathbf{U} / \Pi) = Ra_T \partial_x \theta - Ra_C \partial_x \Theta, \tag{A.3}$$

$$\nabla \cdot \mathbf{U} = 0, \tag{A.4}$$

for the four principle variables: enthalpy \mathcal{H} , concentration Θ , and two components of the flux \mathbf{U} . In these equations, k is the ratio of thermal conductivities, \mathcal{B} is a dimensionless heat transfer coefficient, Le is the Lewis number, Ra_T and Ra_C are thermal and compositional Rayleigh numbers and ∂_x is the partial derivative with respect to x . The dimensionless temperature is θ and we have dropped primes on all dimensionless variables in Eqs. (A.1)–(A.4) and below. Eqs. (1), (5) and (12) become

$$\mathcal{H} = \chi S + [\chi + (1 - \chi)c_p] \theta, \tag{A.5}$$

$$\Theta = \chi \Theta_1 + (1 - \chi) \Theta_s, \tag{A.6}$$

$$\Pi = \left(Da + \frac{\Pi_0}{\Pi_\chi} \right)^{-1}, \tag{A.7}$$

where S is the Stefan number, c_p is the ratio of heat capacities and Da is the Darcy number.

Nondimensionalization of the Enthalpy Method equations results in equations for the liquidus and solidus

$$\theta_L = \Theta_1, \tag{A.8}$$

$$\theta_S = \max[0, p_s^{-1}(\Theta_s - \mathcal{C})] \tag{A.9}$$

and equations for the bounding energies

$$\mathcal{H}_S = c_p \theta_S(\Theta), \tag{A.10}$$

$$\mathcal{H}_E = \chi_e S, \tag{A.11}$$

$$\mathcal{H}_L = S + \theta_L(\Theta), \tag{A.12}$$

where the porosity at the upper limit of the eutectic, χ_e , is given by

$$\chi_e = 1 - \frac{\Theta}{\mathcal{C}}. \tag{A.13}$$

Table A.1
Scalings and nondimensional parameters

$\mathbf{x} = h \mathbf{x}'$	$t = \frac{h^2}{\kappa_1} t'$	$\Pi = \Pi_0 \Pi'$	$(\mathbf{U}, V) = \frac{\kappa_1}{h} (\mathbf{U}', V)'$
$\kappa_1 = \frac{k_1}{\rho c_{p,1}}$	$k = k_s / k_1$	$\Delta T = T_L(C_1) - T_e$	$H = \rho c_{p,1} \Delta T \mathcal{H}'$
$c_p = c_{p,s} / c_{p,1}$	$\theta = \frac{T - T_e}{\Delta T}$	$\mathcal{C} = \frac{c_s c_e - c_e^2}{c_s - c_e}$	$\Theta = \frac{C - c_e}{c_s - c_e}$
$S = \frac{L}{c_{p,1} \Delta T}$	$Le = \kappa_1 / D_1$	$Da = \frac{1/2 \Pi_0}{d^2}$	$\mathcal{B} = bh^2 / k_1$
$Ra_T = \frac{\rho g h \Delta T \Pi_0}{\kappa_1 \eta}$	$Ra_C = \frac{\rho g h (C_1 - C_e) \Pi_0}{\kappa_1 \eta}$		

Table A.2
Dimensionless formulas for Enthalpy Method variables

	(a) Mode	(b) χ	(c) θ	(d) Θ_s	(e) Θ_l
(1)	$\mathcal{H} \leq \mathcal{H}_S$	0	$\frac{\mathcal{H}}{C}$	Θ	N/A
(2)	$\mathcal{H}_S < \mathcal{H} \leq \mathcal{H}_E$	$\frac{\mathcal{H}}{S}$	0	$\frac{\Theta}{(1-\chi)}$	0
(3)	$\mathcal{H}_E < \mathcal{H} < \mathcal{H}_L$	Eq. (A.14)	$\theta_L(\Theta_l)$	$\frac{p_s \Theta - \mathcal{H} \chi}{\chi + p_s(1-\chi)}$	$\frac{\Theta - \mathcal{H}(1-\chi)}{\chi + p_s(1-\chi)}$
(4)	$\mathcal{H} \geq \mathcal{H}_L$	1	$\mathcal{H} - S$	N/A	Θ

Having calculated each of the bounding energies for a given Θ , the Enthalpy Method variables can be calculated according to Table A.2.

When the bulk enthalpy and composition are on the liquidus ($\mathcal{H}_E < \mathcal{H} < \mathcal{H}_L$), the porosity is calculated by combining Eqs. (A.5), (A.6), (A.8) and (A.9),

$$\chi(\mathcal{H}, \Theta) = \frac{-B - (B^2 - 4AC)^{1/2}}{2A}, \tag{A.14}$$

where A, B and C are given by

$$A = \mathcal{C}(c_p - 1) + S(p_s - 1), \tag{A.15}$$

$$B = \mathcal{C}(1 - 2c_p) + \mathcal{H}(1 - p_s) + \Theta(c_p - 1) - p_s S, \tag{A.16}$$

$$C = (\mathcal{C} - \Theta)c_p + p_s \mathcal{H}. \tag{A.17}$$

Appendix B. Discrete equations

As discussed in Section 2.5, we use Newton’s method to solve the nonlinear system of equations resulting from the discretization of the governing PDEs. Newton’s method requires a residual for each variable at each mesh point; these residuals are provided by the discrete equations. In this appendix we present the discrete version of nondimensional Eqs. (A.1)–(A.4). We begin with the conservation of mass and momentum.

For a cell in row i and column j of a staggered mesh, the residual of the conservation of mass equation (A.4) is given by

$$R_{ij}^{Ma} = \frac{U_{ij} - U_{i-1j}}{\Delta x} + \frac{W_{ij} - W_{ij-1}}{\Delta z}. \tag{B.1}$$

This equation is centered at the middle of grid cell ij . The conservation of momentum equation (A.3) for cell ij , in contrast, is centered in the corner of the cell in the direction of increasing i and j . Its residual is given by

$$R_{ij}^{Mo} = Ra_T \frac{\theta_{i+1j} + \theta_{i+1j+1} - \theta_{1,ij} - \theta_{ij+1}}{2\Delta x} - Ra_C \frac{\Theta_{1,i+1j} + \Theta_{1,i+1j+1} - \Theta_{1,ij} - \Theta_{1,ij+1}}{2\Delta x} - \left(\frac{(W/\Pi_N)_{i+1j} - (W/\Pi_N)_{ij}}{\Delta x} - \frac{(U/\Pi_E)_{ij+1} - (U/\Pi_E)_{ij}}{\Delta z} \right), \tag{B.2}$$

where U and W are components of the flux \mathbf{U} . Π_{Nij} is the permeability on the $j+$ edge of cell ij , hence it is calculated from the porosities of cells ij and $ij + 1$ (likewise, Π_{Eij} is on the $i+$ edge). There are six possible ways to calculate the permeability between cells: we can use a mean porosity between two cells to calculate the permeability or we can calculate the permeabilities first and then average; for either of these two choices, we can average using the arithmetic, geometric or harmonic means. The arithmetic mean can be ruled out because it yields nonzero permeability between two cells where one has zero-porosity. We have chosen to use the geometric mean of the permeabilities. The geometric mean equals zero when appropriate and otherwise gives a result that is between the arithmetic mean and the harmonic mean. When the momentum equation stencil lies partially or completely within the zero-porosity/zero-permeability region of the domain, the corresponding velocity components and ratios in Eq. (B.2) are forced to equal zero.

Conservation of energy and bulk composition equations contain time derivatives and thus require discretization in time as well as space. Below we use the notation $\Theta_{1,ij}^n$ to denote the value of the dimensionless concentration in the liquid at time $t_n = \sum_{k=1}^n \Delta t_k$, where the length of each time-step Δt_k varies in inverse proportion to $\max |\mathbf{U}|$. We use a semi-implicit discretization and hence discretize terms in Eqs. (A.1) and (A.2) at $t_{n+1/2}$, e.g. $\Theta_{1,ij}^{n+1/2} = 1/2(\Theta_{1,ij}^{n+1} + \Theta_{1,ij}^n)$. The discrete residual of conservation of energy is

$$R_{ij}^{En} = \frac{\mathcal{H}_{ij}^{n+1} - \mathcal{H}_{ij}^n}{\Delta t_n} + \mathcal{D}_A(\theta_{i\pm 2j\pm 2}^{n+1/2}) - \mathcal{D}_D(\chi_{i\pm 1j\pm 1}^{n+1/2}, \theta_{i\pm 1j\pm 1}^{n+1/2}) + \mathcal{B}(\theta_{ij}^{n+1/2} - \theta_\infty), \tag{B.3}$$

where \mathcal{D}_A and \mathcal{D}_D are the discrete advection and diffusion operators, discussed below. The Lagrangian derivative in Eq. (A.1), which derives from the downward translation of the Hele-Shaw cell at a rate V , is discretized with a semi-Lagrangian ap-

proach [40,39]; enthalpy at t_n is not evaluated at cell ij , but rather at point ij^* , where j^* is, in general, not an integer. This is the foot of the characteristic that ends at cell ij at time t_{n+1} . The position of the foot is given by $j^* = j + V\Delta t_n/\Delta z$. The value of the enthalpy (or bulk composition, see below) there is determined by cubic interpolation.

The discrete equation for the residual of conservation of bulk composition is

$$R_{ij}^{\text{Co}} = \frac{\Theta_{ij}^{n+1} - \Theta_{ij}^n}{\Delta t_n} + \mathcal{D}_A(\Theta_{1,i\pm 2j\pm 2}^{n+1/2}) - Le^{-1} \mathcal{D}_D(\chi_{1,i\pm 1j\pm 1}^{n+1/2}, \Theta_{1,i\pm 1j\pm 1}^{n+1/2}), \quad (\text{B.4})$$

where, again, we have used a semi-Lagrangian discretization of the Lagrangian time derivative and a semi-implicit formulation of the other terms. The discrete advection operator \mathcal{D}_A is constructed using the Fromm scheme, a second-order upwind method with a nine-point, star-shaped stencil [1,43]. The discrete diffusion operator \mathcal{D}_D is discretized using the standard finite difference five-point stencil with porosity averaged arithmetically to calculate diffusivity at the cell edges.

Each evaluation of Eqs. (B.3) and (B.4) requires values for the temperature, porosity and liquid composition that are locally consistent with enthalpy and bulk composition. These are calculated with constitutive equations derived from the Enthalpy Method, given in Table A.2. Upon convergence of the energy–concentration solver, enthalpy, bulk composition, temperature, porosity and the phase compositions are all entirely self-consistent and in equilibrium as prescribed by the phase diagram.

References

- [1] M. Albers, A local mesh refinement multigrid method for 3-D convection problems with strongly variable viscosity, *J. Comput. Phys.* 160 (2000) 126–150.
- [2] V. Alexiades, A.D. Solomon, *Mathematical Modeling of Melting and Freezing Processes*, Hemisphere Publishing Corporation, 1993.
- [3] P. Aussillous, A.J. Sederman, L.F. Gladden, H.E. Huppert, M.G. Worster, Magnetic resonance imaging of structure and convection in solidifying mushy layers, *J. Fluid Mech.* 552 (2006) 99–125.
- [4] S. Balay, K. Buschelman, W.D. Gropp, D. Kaushik, M. Knepley, L. Curfman McInnes, B.F. Smith, H. Zhang, *PETSc users manual*. Technical Report ANL-95/11 – Revision 2.1.5, Argonne National Laboratory, 2002.
- [5] S. Balay, K. Buschelman, W.D. Gropp, D. Kaushik, M. Knepley, L.C. McInnes, B.F. Smith, H. Zhang, *PETSc home page*. <<http://www.mcs.anl.gov/petsc>>, 2001.
- [6] S. Balay, W.D. Gropp, L. Curfman McInnes, B.F. Smith, Efficient management of parallelism in object oriented numerical software libraries, in: E. Arge, A.M. Bruaset, H.P. Langtangen (Eds.), *Modern Software Tools in Scientific Computing*, Birkhäuser Press, 1997, pp. 163–202.
- [7] J. Bear, *Dynamics of Fluids in Porous Media*, Elsevier, 1972.
- [8] C. Beckermann, C.Y. Wang, Multiphase/-scale modeling of alloy solidification, in: C. Tien (Ed.), *Annual Review of Heat Transfer*, vol. 6, Begell House Inc., 1995, pp. 115–198 [Chapter 3].
- [9] C. Beckermann, H.J. Diepers, I. Steinbach, A. Karma, X. Tong, Modeling melt convection in phase-field simulations of solidification, *J. Comput. Phys.* 154 (1999) 468–496.
- [10] M.I. Bergman, D.R. Fearn, J. Bloxham, M.C. Shannon, Convection and channel formation in solidifying Pb–Sn alloys, *Metall. Mater. Trans. A–Phys. Metall. Mater. Sci.* 28 (3A) (1997) 859–866.
- [11] W.J. Boettinger, J.A. Warren, C. Beckermann, A. Karma, Phase-field simulation of solidification, *Ann. Rev. Mater. Res.* 32 (2002) 163–194.
- [12] X.D. Cai, D. Keyes, V. Venkatakrishnan, Newton–Krylov–Schwartz: an implicit solver for CFD, in: *Proceedings of the Eighth International Conference on Domain Decomposition Methods*, 1997, pp. 387–400.
- [13] C.F. Chen, Experimental study of convection in a mushy layer during directional solidification, *J. Fluid Mech.* 293 (1995) 81–98.
- [14] A.O.P. Chiarelli, H.E. Huppert, M.G. Worster, Segregation and flow during the solidification of alloys, *J. Cryst. Growth* 139 (1994) 134–146.
- [15] A.O.P. Chiarelli, M.G. Worster, Flow focusing instability in a solidifying mushy layer, *J. Fluid Mech.* 297 (1995) 293–305.
- [16] C.A. Chung, M.G. Worster, Steady-state chimneys in a mushy layer, *J. Fluid Mech.* 455 (2002) 387–411.
- [17] S.M. Copley, A.F. Giamei, S.M. Johnson, M.F. Hornbecker, Origin of freckles in unidirectionally solidified castings, *Metall. Trans.* 1 (8) (1970) 2193.
- [18] J.W. Demmel, *Applied numerical linear algebra*, SIAM (1997).
- [19] A.C. Fowler, The formation of freckles in a binary alloy, *IMA J. Appl. Math.* 35 (1985) 159–174.
- [20] J. Happel, H. Brenner, *Low Reynolds Number Hydrodynamics: With Special Applications to Particulate Media*. Mechanics of Fluids and Transport Processes, Springer, 1981.
- [21] R.N. Hills, D.E. Loper, P.H. Roberts, A thermodynamically consistent model of a mushy zone, *Q. J. Mech. Appl. Math.* 36 (1983) 505–539.
- [22] J. Jain, A. Kumar, P. Dutta, Role of plume convection and remelting on the mushy layer structure during directional solidification, *J. Phys. D Appl. Phys.* 40 (4) (2007) 1150–1160.
- [23] R.F. Katz, M. Knepley, B. Smith, M. Spiegelman, E. Coon, Numerical simulation of geodynamic processes with the Portable Extensible Toolkit for Scientific Computation, *Phys. Earth Planet. In.* 163 (2007) 52–68.
- [24] B.H. Kear, *Advanced metals*, *Sci. Amer.* 255 (1986) 159–187.
- [25] D.A. Knoll, D.B. Kothe, B. Lally, A new nonlinear solution method for phase-change problems, *Numer. Heat Transfer B – Fundam.* 35 (4) (1999) 439–459.
- [26] G. Lauriat, V. Prasad, Non-Darcian effects on natural convection in a vertical porous enclosure, *Int. J. Heat Mass Transfer* 32 (1989) 2135–2148.
- [27] M. Le Bars, M.G. Worster, Interfacial conditions between a pure fluid and a porous medium: implications for binary alloy solidification, *J. Fluid Mech.* 550 (2006) 149–173.
- [28] M. Le Bars, M.G. Worster, Solidification of a binary alloy: finite-element, single-domain simulation and new benchmark solutions, *J. Comput. Phys.* 216 (2006) 247–263.
- [29] D.E. Loper, P.H. Roberts, Mush-chimney convection, *Stud. Appl. Math.* 106 (2001) 187–227.
- [30] W.W. Mullins, R.F. Sekerka, Stability of a planar interface during solidification of a dilute binary alloy, *J. Appl. Phys.* 35 (1964) 444–451.
- [31] P. Nithiarasu, K.N. Seetharamu, T. Sundararajan, Natural convective heat transfer in an enclosure filled with fluid saturated variable porosity medium, *Int. J. Heat Mass Transfer* 40 (1997) 3955–3967.
- [32] A.B. Oertling, R.G. Watts, Growth of and brine drainage from NaCl–H₂O freezing: a simulation of young sea ice, *J. Geophys. Res. Ocean* (2004) 109.
- [33] S.S.L. Peppin, P. Aussillous, H.E. Huppert, M.G. Worster, Steady-state mushy layers: experiments and theory, *J. Fluid Mech.* 570 (2007) 69–77.
- [34] S.S.L. Peppin, H.E. Huppert, M.G. Worster, Steady-state solidification of aqueous ammonium chloride, *J. Fluid Mech.* 599 (2008) 465–476.
- [35] Y. Saad, M.H. Schultz, GMRES – a generalized minimal residual algorithm for solving nonsymmetric linear-systems, *SIAM J. Sci. Stat. Comp.* 7 (3) (1986) 856–869.
- [36] T.P. Schulze, M.G. Worster, A numerical investigation of steady convection in mushy layers during the directional solidification of binary alloys, *J. Fluid Mech.* 356 (1998) 199–220.
- [37] T.P. Schulze, M.G. Worster, Weak convection, liquid inclusions and the formation of chimneys in mushy layers, *J. Fluid Mech.* 388 (1999) 197–215.

- [38] W. Shyy, H.S. Udaykumar, Madhukar M. Rao, R.W. Smith, *Computational fluid dynamics with moving boundaries*, Series in Computational and Physical Processes in Mechanics and Thermal Sciences, Taylor & Francis, 1996.
- [39] M. Spiegelman, R.F. Katz, A semi-Lagrangian Crank–Nicolson algorithm for the numerical solution of advection–diffusion problems, *Geochem. Geophys. Geosys.* 7 (Q04014) (2006).
- [40] A. Staniforth, J. Cote, Semi-lagrangian integration schemes for atmospheric models—a review, *Mon. Weather Rev.* 119 (1991) 2206–2223.
- [41] S. Tait, K. Jahrling, C. Jaupart, The planform of compositional convection and chimney formation in a mushy layer, *Nature* 359 (6394) (1992) 406–408.
- [42] S. Tait, C. Jaupart, Compositional convection in a reactive crystalline mush and melt differentiation, *J. Geophys. Res.* 97 (B5) (1992) 6735–6756.
- [43] R.A. Trompert, U. Hansen, The application of a finite volume multigrid method to 3d flow problems in a highly viscous fluid with variable viscosity, *Geophys. Astrophys. Fluid Dyn.* 83 (1996) 261.
- [44] J.S. Wettlaufer, M.G. Worster, H.E. Huppert, Natural convection during solidification of an alloy from above with application to the evolution of sea ice, *J. Fluid Mech.* 344 (1997) 291–316.
- [45] S.H. Whiteoak, H.E. Huppert, M.G. Worster, Conditions for defect-free solidification of aqueous ammonium chloride in a quasi two-dimensional directional solidification facility, *J. Cryst. Growth* 310 (15) (2008) 3545–3551.
- [46] M.G. Worster, Natural convection in a mushy layer, *J. Fluid Mech.* 224 (1991) 335–359.
- [47] M.G. Worster, Instabilities of the liquid and mushy regions during solidification of alloys, *J. Fluid Mech.* 237 (1992) 649–669.
- [48] M.G. Worster, Convection in mushy layers, *Ann. Rev. Fluid Mech.* 29 (1997) 91–122.
- [49] M.G. Worster, Solidification of fluids, in: H.K. Moffatt, G.K. Batchelor, M.G. Worster (Eds.), *Perspectives in Fluid Dynamics – a Collective Introduction to Current Research*, Cambridge University Press, 2000, pp. 393–446.
- [50] N. Zabarvas, D. Samanta, A stabilized volume-averaging finite element method for flow in porous media and binary alloy solidification, *Int. J. Numer. Meth. Eng.* 60 (2004) 1103–1138.